Numerical solutions on fracture of piezoelectric materials by hybrid element

C. C. Wu[a] K. Y. Sze[b] Y. Q. Huang[a]

a *Department of Modern Mechanics, University of Science & Technology of China, Hefei 230026, China*

b *Department of Mechanical Engineering, The University of Hong Kong, Hong Kong, China*

Abstract

The cracked piezoelectric problem is observed numerically. To simulate the characteristic singularity at the crack tip, a plane piezoelectric hybrid element is derived. The new model involves displacement $\boldsymbol{u}$, stress $\boldsymbol{\sigma}$, electric displacement $\boldsymbol{D}$ and electric potential φ as the independent variables. The electromechanical coupling behavior of the cracked piezoelectric ceramics PZT-4 and PZT-5 is investigated. Under impermeable crack condition, the $1/\sqrt{r}$ -singularity at the crack tip zone is exactly represented for $\boldsymbol{\sigma}$ and $\boldsymbol{D}$. The efficiency of implementing the permeable crack condition is also inspected. To examine current energy release rate formulas, the path-independent integral is computed, and then a fitting formula for the energy release rate is obtained. In the paper, all the numerical results are compared with the previously reported theoretical solutions.

Published in *Inter.J.Solids & Structures* **38**: 4315-4329 (2001).

1. Introduction

Piezoelectric ceramics has been indispensable for electromechanical transducers, sensors, actuators and adaptive structures as well as various resonators. Piezoelectric ceramics are brittle in nature. When subjected to loading, these materials can fail prematurely due to the propagation of flaws or defects induced during the manufacturing process and by the in-service electromechanical loading. Hence, it is important to understand and be able to analyse the fracture characteristics of piezoelectric materials so that reliable service life predictions of the pertinent devices can be conducted.

Among the theoretical studies of cracked piezoelectric bodies, Permeable (see Parton, 1976) and impermeable (see Deeg, 1980) conditions at the crack face are mostly adopted. Under Parton's permeable condition, the electric potential and the normal component of the electric displacement are assumed to be continuous across the crack. This is considered to be acceptable for slender cracks in which the separation between the faces is negligible. Deeg's impermeable condition is based on the observation that the permitivity of air/vacuum is typically three order of magnitude lower than that of the piezoelectric materials. The crack cavity induces an insulating condition in which the normal component of the electric displacement vanish. In other words, the crack face is charge-free. However, the exact or most realistic interfacial conditions at the crack face (in between material and air/vacuum) should be the continuities of the normal component of the electric displacement and the tangential component of the electric field (see Jackson, 1976).

Using Deeg's impermeable condition, Pak (1990) derived the closed-form solutions for model III crack by the semi-inverse method and proposed a path independent integral for computing the energy release rate by Eshelby's method. Later, Pak (1992) used the method of distributed dislocations and electric dipoles to calculated the electro-elastic fields for anti-plane and plane strain cracks in infinite piezoelectric bodies subjected to far-field electromechanical loads. Using Stroh's formalism, Park and Sun (1995) presented the full field closed-form solutions for all the three modes of fracture for an insulated crack embedding in an infinite piezoelectric medium. The formulae for the energy release rates of PZT-5 and PZT-4 piezoelectric ceramics were also worked out respectively by Pak (1992) and Park & Sun (1995). It is worthnoting that the electric loading always resists the crack from propagation when energy release rate is the governing fracture criteria. This contradicts with the experimental evident that electric field can both impede and promote crack propagation. Based on the conjecture that fracture is purely a mechanical phenomenon, Park and Sun (1995) proposed to adopt the strain energy release rate as the fracture criterion. Sosa (1992) again employed Deeg's impermeable condition to derive the asymptotic expressions for the electromechanical fields near the crack tip in an infinite plane strain body using complex potentials. The characteristic singularity at the crack tip for all variables was

found to be $1/\sqrt{r}$ and the angular distributions of stress and electric displacement at the crack tip zone depend not only on the geometry and loading, but also on the material properties. The results of Pak (1992), Park & Sun (1995) and Sosa (1992) all indicate that the maximum circumferential or crack opening stress does not occur at the angular position in line with the crack when the electric loading is sufficiently large. This agrees with the experimental observation of crack deviating from the original crack line.

Dunn (1994) considered both Parton's permeable and Deeg's impermeable conditions, significant difference was noted in the energy release rate. Using the exact interfacial conditions at the elliptic cavity face, Sosa & Khutoryansky (1996) re-examined the closed form expressions for the elastic and electric variables induced inside and outside the cavity in a plane strain infinite body. They found that the electric fields at the crack tip are large but not singular. It was also pointed out that the impermeable condition would lead to significant error for slender ellipses or sharp cracks.

Compared to the amount of theoretical works, numerical studies of cracked piezoelectric bodies are rare. Kumar & Singh (1996) studied the double-edge cracked PZT-5 panel using the eight-node element. Although the computed $\sigma_r\sqrt{r}$, $\sigma_\theta\sqrt{r}$, $\tau_{r\theta}\sqrt{r}$, $D_r\sqrt{r}$ and $D_\theta\sqrt{r}$ at the crack tip zone always change with respect to the distance from the crack tip and the analytical $1/\sqrt{r}$ -singularity cannot be confirmed, the numerical results at some particular radius are close to the theoretical predictions of Pak (1992). Later, Kumar & Singh (1997) also studied a centrally cracked panel. They examined the angular distribution of the circumference stress and energy release rates at the crack-tip zone under electromechanical loading. Substantial difference was noted in the predicted directions of crack propagation when stress- and energy-based fracture criteria were used.

In this paper, a four-node plane piezoelectric hybrid finite element mode which is markedly more accurate than its standard one will be derived using a multi-field functional that involves displacement, electric potential, stress and electric displacement as the independent variables.

With the new finite element model, the effect of Parton's permeable and Deeg's impermeable conditions on the crack tip solution is studied. The path-independent *J*-integral is also calculated so as to examine the influence of the electric loading on the energy release rate.

2. Constitutive relations and variational functional

In most publications (see Pak, 1990, 1992; Park & Sun, 1995; Kumar & Singh, 1996, 1997), constitutive constants for transverse isotropic piezoelectric materials like PZT-4 and PZT-5 are given with respect to the following relations:

$$\begin{Bmatrix} \sigma_{11} \\ \sigma_{22} \\ \sigma_{33} \\ \sigma_{32} \\ \sigma_{31} \\ \sigma_{12} \end{Bmatrix} = \begin{bmatrix} C_{11} & C_{12} & C_{13} & 0 & 0 & 0 \\ C_{12} & C_{11} & C_{13} & 0 & 0 & 0 \\ C_{13} & C_{13} & C_{33} & 0 & 0 & 0 \\ 0 & 0 & 0 & C_{44} & 0 & 0 \\ 0 & 0 & 0 & 0 & C_{44} & 0 \\ 0 & 0 & 0 & 0 & 0 & (C_{11}-C_{12})/2 \end{bmatrix} \begin{Bmatrix} \varepsilon_{11} \\ \varepsilon_{22} \\ \varepsilon_{33} \\ 2\varepsilon_{32} \\ 2\varepsilon_{31} \\ 2\varepsilon_{12} \end{Bmatrix} - \begin{bmatrix} 0 & 0 & e_{31} \\ 0 & 0 & e_{31} \\ 0 & 0 & e_{33} \\ 0 & e_{15} & 0 \\ e_{15} & 0 & 0 \\ 0 & 0 & 0 \end{bmatrix} \begin{Bmatrix} E_1 \\ E_2 \\ E_3 \end{Bmatrix} \tag{1}$$

and

$$\begin{Bmatrix} D_1 \\ D_2 \\ D_3 \end{Bmatrix} = \begin{bmatrix} 0 & 0 & 0 & 0 & e_{15} & 0 \\ 0 & 0 & 0 & e_{15} & 0 & 0 \\ e_{31} & e_{31} & e_{33} & 0 & 0 & 0 \end{bmatrix} \begin{Bmatrix} \varepsilon_{11} \\ \varepsilon_{22} \\ \varepsilon_{33} \\ 2\varepsilon_{32} \\ 2\varepsilon_{31} \\ 2\varepsilon_{12} \end{Bmatrix} + \begin{bmatrix} \in_{11} & 0 & 0 \\ 0 & \in_{11} & 0 \\ 0 & 0 & \in_{33} \end{bmatrix} \begin{Bmatrix} E_1 \\ E_2 \\ E_3 \end{Bmatrix} \tag{2}$$

in which the 1-2-plane is the plane symmetry and 3 is the poling direction, σ_{ij} and ε_{ij} are the stress and the strain tensors, E_i and D_i are the electric field strength and electric displacement vectors, C_{ij} are the material elasticity constants measured at constant electric field, $\in_{ij}$ are the dielectric constants measured at constant strain and e_{ij} are the piezoelectric constants. After incorporating the plane strain assumptions and taking y-axes as the poling direction, the constitutive relations can be degenerated and expressed in the following forms:

$$\begin{Bmatrix} \varepsilon_x \\ \varepsilon_y \\ \gamma_{xy} \end{Bmatrix} = \begin{bmatrix} S_{11} & S_{12} & 0 \\ S_{12} & S_{22} & 0 \\ 0 & 0 & S'_{33} \end{bmatrix} \begin{Bmatrix} \sigma_x \\ \sigma_y \\ \tau_{xy} \end{Bmatrix} + \begin{bmatrix} 0 & g_{21} \\ 0 & g_{22} \\ g_{13} & 0 \end{bmatrix} \begin{Bmatrix} D_x \\ D_y \end{Bmatrix} \quad \text{or} \quad \boldsymbol{\varepsilon} = \mathbf{S}\boldsymbol{\sigma} + \mathbf{g}^T\mathbf{D} \tag{3}$$

and

$$\begin{Bmatrix} E_x \\ E_y \end{Bmatrix} = -\begin{bmatrix} 0 & 0 & g_{13} \\ g_{21} & g_{22} & 0 \end{bmatrix} \begin{Bmatrix} \sigma_x \\ \sigma_y \\ \tau_{xy} \end{Bmatrix} + \begin{bmatrix} f_1 & 0 \\ 0 & f_2 \end{bmatrix} \begin{Bmatrix} D_x \\ D_y \end{Bmatrix} \quad \text{or} \quad \mathbf{E} = -\mathbf{g}\boldsymbol{\sigma} + \mathbf{f}\,\mathbf{D} \tag{4}$$

in which all symbols are self-defined. Furthermore, the strain-displacement relation and electric field-electric potential relation are:

$$\begin{Bmatrix} \varepsilon_x \\ \varepsilon_y \\ \gamma_{xy} \end{Bmatrix} = \begin{bmatrix} \partial/\partial x & 0 \\ 0 & \partial/\partial y \\ \partial/\partial y & \partial/\partial x \end{bmatrix} \begin{Bmatrix} u \\ v \end{Bmatrix} \text{or}\, \boldsymbol{\varepsilon} = \mathcal{D}_m \mathbf{u} \tag{5}$$

and

$$\begin{Bmatrix} E_x \\ E_y \end{Bmatrix} = -\begin{bmatrix} \partial/\partial x \\ \partial/\partial y \end{bmatrix}\varphi \quad \text{or} \quad \mathbf{E} = -\mathcal{D}_e\varphi \tag{6}$$

where φ is the electric potential and all other symbols are self-defined. The following multifield variational functional for plane piezoelectricity is considered (see EerNisse, 1983):

$$\Pi(\mathbf{u},\varphi,\boldsymbol{\sigma},\mathbf{D}) = \int_V (h_m + \boldsymbol{\sigma}^T \mathcal{D}_m\mathbf{u} + \mathbf{D}^T\mathcal{D}_e\varphi)dv - \int_{S_\sigma} \overline{\mathbf{T}}^T\mathbf{u}ds - \int_{S_\varpi} \overline{\omega}^T\varphi ds \tag{7}$$

where

V denotes the domain of the two-dimensional body

$h_m = -\frac{1}{2}\boldsymbol{\sigma}^T\boldsymbol{S}\boldsymbol{\sigma} - \boldsymbol{\sigma}^T\boldsymbol{g}^T\boldsymbol{D} + \frac{1}{2}\boldsymbol{D}^T\boldsymbol{f}\boldsymbol{D}$ is the mechanical enthalpy

S_σ denotes the boundary portion that the prescribed traction $\overline{\mathbf{T}}$ is acting

S_ω denotes the boundary portion that the prescribed surface charge density $\overline{\omega}$ is acting

Euler's equations for the functional are:

Stress equilibrium condition: $\mathcal{D}_m^T\boldsymbol{\sigma} = \mathbf{0}$ in V (8)

Charge conservation condition: $\mathcal{D}_e^T\mathbf{D} = \mathbf{0}$ in V (9)

Constitutive relations: $\mathcal{D}_m\mathbf{u} = \mathbf{S}\boldsymbol{\sigma} + \mathbf{g}^T\mathbf{D}$, $\mathcal{D}_e\varphi = -\mathbf{g}\boldsymbol{\sigma} + \mathbf{f}\,\mathbf{D}$ in V (10)

Mechanical natural boundary condition: $\mathbf{n}_m\boldsymbol{\sigma} = \overline{\mathbf{T}}$ at S_σ (11)

Electric natural boundary condition: $\mathbf{n}_e\mathbf{D} = -\overline{\omega}$ at S_ϖ (12)

where

$$\mathbf{n}_m = \begin{bmatrix} n_x & 0 & n_y \\ 0 & n_y & n_x \end{bmatrix} \text{ and } \mathbf{n}_e = [n_x \quad n_y] \tag{13}$$

in which (n_x, n_y) constitute the outward normal of the domain boundary. It can be shown that the subsidiary conditions of the functional are strain-displacement relation, electric field-electric potential relation, the mechanical essential boundary condition (displacement prescribed) and electric essential boundary condition (electric potential prescribed).

3. Finite element formulation

Four-node elements are very popular in finite element analysis due to its good balance of accuracy, computational cost and the small bandwidth/frontwidth arisen. However, the standard isoparametric

element is rather poor. In this section, a four-node plane piezoelectric element will be developed based on the functional given in Eqn.(7), see Fig.1. The nodal d.o.f.s include the two displacement components and the electric potential. They and the co-ordinates are interpolated, i.e.

$$\begin{Bmatrix} u \\ v \\ \varphi \end{Bmatrix} = \frac{1}{4}\sum_{i=1}^{4}(1+\xi_i\xi)(1+\eta_i\eta)\begin{Bmatrix} u_i \\ v_i \\ \varphi_i \end{Bmatrix} = \mathbf{N}\,\mathbf{q} \quad \text{and} \quad \begin{Bmatrix} x \\ y \end{Bmatrix} = \frac{1}{4}\sum_{i=1}^{4}(1+\xi_i\xi)(1+\eta_i\eta)\begin{Bmatrix} x_i \\ y_i \end{Bmatrix} \tag{14}$$

where the variables with subscripts denote their nodal values, ξ and η bounded by -1 and +1 are the natural coordinates. Moreover,

$$\mathbf{N} = \frac{1}{4}\left[(1-\xi)(1-\eta)\mathbf{I}_3 \quad (1+\xi)(1-\eta)\mathbf{I}_3 \quad (1+\xi)(1+\eta)\mathbf{I}_3 \quad (1-\xi)(1+\eta)\mathbf{I}_3\right] \tag{15}$$

$$\mathbf{q} = \{u_1, v_1, \varphi_1, \ldots, u_4, v_4, \varphi_4\}^T \tag{16}$$

The stress field of Pian-Sumihara element is employed (see Pian & Sumihara, 1984), i.e.

$$\begin{Bmatrix} \sigma_x \\ \sigma_y \\ \tau_{xy} \end{Bmatrix} = \begin{bmatrix} 1 & 0 & 0 & a_3^2\xi & a_1^2\eta \\ 0 & 1 & 0 & b_3^2\xi & b_1^2\eta \\ 0 & 0 & 1 & a_3b_3\xi & a_1b_1\eta \end{bmatrix}\begin{Bmatrix} \beta_1 \\ \vdots \\ \beta_5 \end{Bmatrix} = \mathbf{P}_m\,\boldsymbol{\beta}_m \tag{17}$$

in which the geometric parameters are :

$$\begin{bmatrix} a_1 & b_1 \\ a_2 & b_2 \\ a_3 & b_3 \end{bmatrix} = \frac{1}{4}\begin{bmatrix} -1 & 1 & 1 & -1 \\ 1 & -1 & 1 & -1 \\ -1 & -1 & 1 & 1 \end{bmatrix}\begin{bmatrix} x_1 & y_1 \\ x_2 & y_2 \\ x_3 & y_3 \\ x_4 & y_4 \end{bmatrix} \tag{18}$$

The element stress (17) can be degenerated from uncoupled complete linear expansions by the mechanical energy consistency condition (see Pian & Wu, 1988; Wu & Cheung, 1995).

For the element electric displacement, it is initially assumed as a linear function:

$$\boldsymbol{D} = \begin{Bmatrix} D_x \\ D_y \end{Bmatrix} = \left[\begin{array}{cc|cccc} 1 & 0 & \xi & \eta & 0 & 0 \\ 0 & 1 & 0 & 0 & \xi & \eta \end{array}\right] \begin{Bmatrix} \beta_1 \\ \beta_2 \\ \hline \beta_3 \\ \vdots \\ \beta_6 \end{Bmatrix} = \boldsymbol{D}_c + \boldsymbol{D}_h \tag{19}$$

where $\boldsymbol{D}_c$ and $\boldsymbol{D}_h$ are the constant mode and the high order mode respectively. For purpose of improving numerical performance of the piezoelectric hybrid element, the electric energy consistency condition (see Liu, 1998) will be introduced into $\boldsymbol{D}_h$. Such that two β-parameters will be eliminated from Eqn. (19), and the desirable electric displacement can be formulated as

$$\begin{Bmatrix} D_x \\ D_y \end{Bmatrix} = \begin{bmatrix} 1 & 0 & a_3\xi & a_1\eta \\ 0 & 1 & b_3\xi & b_1\eta \end{bmatrix} \begin{Bmatrix} \beta_6 \\ \vdots \\ \beta_9 \end{Bmatrix} = \mathbf{P}_e \boldsymbol{\beta}_e \tag{20}$$

For finite element formulation, the functional given in Eqn.(7) is re-written as :

$$\Pi(\mathbf{u}, \varphi, \boldsymbol{\sigma}, \mathbf{D}) = \sum_{elements} \Pi^e(\mathbf{u}^e, \varphi^e, \boldsymbol{\sigma}^e, \mathbf{D}^e) \tag{21}$$

where

$$\Pi^e(\mathbf{u}^e, \varphi^e, \boldsymbol{\sigma}^e, \mathbf{D}^e) = \int_{V^e} (h_m^e + (\boldsymbol{\sigma}^e)^T \mathcal{D}_m \mathbf{u}^e + (\mathbf{D}^e)^T \mathcal{D}_e \varphi^e) dv - \int_{S_\sigma^e} \overline{\mathbf{T}}^T \mathbf{u}^e ds - \int_{S_\omega^e} \overline{\omega}^T \varphi^e ds \tag{22}$$

is the elementwise functional. The superscript "e" denotes an individual element. After invoking Eqn.(14), Eqn.(17) and Eqn.(20), the elementwise functional becomes :

$$\Pi^e = -\frac{1}{2} \begin{Bmatrix} \boldsymbol{\beta}_m \\ \boldsymbol{\beta}_e \end{Bmatrix}^T \mathbf{H} \begin{Bmatrix} \boldsymbol{\beta}_m \\ \boldsymbol{\beta}_e \end{Bmatrix} + \begin{Bmatrix} \boldsymbol{\beta}_m \\ \boldsymbol{\beta}_e \end{Bmatrix}^T \mathbf{G}\,\mathbf{q} - \text{load terms} \tag{23}$$

where

$$\mathbf{H} = \int_{V^e} \begin{bmatrix} \mathbf{P}_m & \mathbf{0}_{3\times4} \\ \mathbf{0}_{2\times5} & \mathbf{P}_e \end{bmatrix}^T \begin{bmatrix} \mathbf{S} & \mathbf{g}^T \\ \mathbf{g} & -\mathbf{f} \end{bmatrix} \begin{bmatrix} \mathbf{P}_m & \mathbf{0}_{3\times4} \\ \mathbf{0}_{2\times5} & \mathbf{P}_e \end{bmatrix} dv\,,$$

$$\mathbf{G} = \int_{V^e} \begin{bmatrix} \mathbf{P}_m & \mathbf{0}_{3\times4} \\ \mathbf{0}_{2\times5} & \mathbf{P}_e \end{bmatrix}^T \left(\begin{bmatrix} \mathcal{D}_m & \mathbf{0}_{3\times1} \\ \mathbf{0}_{2\times2} & \mathcal{D}_e \end{bmatrix} \mathbf{N} \right) dv$$

As the stationary condition of Π, we have

$$\mathbf{H}\begin{Bmatrix}\boldsymbol{\beta}_m\\ \boldsymbol{\beta}_e\end{Bmatrix} = \mathbf{G}\,\mathbf{q} \quad \text{and thus} \quad \Pi^e = \frac{1}{2}\mathbf{q}^T(\mathbf{G}^T\mathbf{H}^{-1}\mathbf{G})\,\mathbf{q} - \text{load terms} \tag{24}$$

Hence, The generalized element matrix is $\mathbf{G}^T\mathbf{H}^{-1}\mathbf{G}$. The element stress and electric displacement can be retrieved by using Eqn.(17), Eqn.(20) and Eqn.(24) after solving $\mathbf{q}$.

Table 1. Material constants for PZT-4 (see Park & Sun, 1995) and PZT-5 (see Pak, 1992) where C_{ij}'s are in $10\,\mathrm{GNm}^{-2}$, e_{ij}'s are in Cm^{-2} and $\in_{ij}$'s are $\mu\mathrm{CV}^{-1}\mathrm{m}^{-1}$.

	C_{11}	C_{12}	C_{13}	C_{33}	C_{44}	e_{31}	e_{33}	e_{15}	$\in_{11}$	$\in_{33}$
PZT-4	13.9	7.78	7.43	11.3	2.56	-6.98	13.84	13.44	6.00	5.47
PZT-5	12.6	5.5	5.3	11.7	3.53	-6.5	23.3	17.0	15.1	13.0

To demonstrate the relative accuracy of the present hybrid element and the standard four-node (Q4) element, the PZT-4 plane strain cantilever depicted in Fig.2 is considered. The cantilever is modeled by ten elements and is subjected to a end moment. Electric potential along the bottom face is set to zero. While the analytic bending stress is a linear function of y, both the analytic deflection and electric potential are quadratic functions of y. Table 2 lists the computed deflection and electric potential at C as well as the computed bending stresses at A and B. The present element model is much more accurate than the standard one.

Table 2. Predictions stress, deflection and electric potential for the cantilever beam shown in Fig.2.

	v^C	φ^C	σ_x^A	σ_x^B	τ_{xy}^A	τ_{xy}^B
Q4	0.755×10^{-6}	-13.84	2843	-2359	-97.65	197.7
present	1.141×10^{-6}	-27.12	3012	-3021	6.960	-29.62
theory	1.184×10^{-6}	-26.67	3000	-3000	0	0

It is noteworthy that the element computational cost can be reduced by replacing ξ and η in Eqn.(17) and Eqn.(20) with

$$\xi' = \xi - \frac{a_1b_2 - a_2b_1}{3(a_1b_3 - a_3b_1)} \quad \text{and} \quad \eta' = \eta - \frac{a_2b_3 - a_3b_2}{3(a_1b_3 - a_3b_1)}\ , \tag{25}$$

respectively. The volume integrals of the above two terms are equal to zero. This induces large sparsity in the H-matrix and thus save a substantial portion of algebraic operations (see Sze, 1992).

4. Numerical analyses and discussions

In this section, the effect of permeable and impermeable conditions on the crack tip solution is

studied with the afore-derived finite element model. From here onward, permeable and impermeable conditions abbreviate respectively Parton's permeable and Deeg's impermeable conditions for simplicity. Pure mechanical, pure electric and mixed loading are considered. The path-independent *J*-integral is also calculated so as to examine the influence of the far field electromechanical loading on the energy release rate. Results are compared with the previously reported theoretical solutions.

To mimic a cracked infinite plate subjected to far field electromechanical loading using finite element method, we consider the centrally cracked plane strain panel depicted in Fig.3. The panel dimension is $2w\times2w$, the half crack length is a and $w/a = 8$. The y-direction far field stress σ_∞ and electric displacement D_∞ are considered. Furthermore, the poling direction is also aligned with the y-axis. It has been checked that the crack tip finite element solution remains virtually unchanged for larger w/a. Owing to symmetry, a quarter of the panel is modeled. Fig.4 and Fig.5 give the details of the finite element mesh. The mesh involves 702 elements and 760 nodes. To capture the strong gradients expected at the crack tip zone, high mesh density is employed as portrayed in Fig.5. The side length for the elements at the crack tip is around $10^{-5}a$. Fig.4 also shows the three different paths along which *J*-integrals are computed. The boundary conditions at the crack faces for the permeable and impermeable conditions are:

Impermeable: $\sigma_y = \tau_{xy} = 0$ and $D_y = 0$

Permeable: $\sigma_y = \tau_{xy} = 0$, $\varphi\big|_{y=0^-} = \varphi\big|_{y=0^+}$ and $D_y\big|_{y=0^-} = D_y\big|_{y=0^+}$

<u>*Pure Mechanical Loading*</u> - In this case, only the far field stress σ_∞ is acting. Fig.6 and Fig.7 show the angular distributions of $\sigma_r\sqrt{r}$, $\sigma_\theta\sqrt{r}$ and $\tau_{r\theta}\sqrt{r}$ for PZT-4 and PZT-5 at the crack tip region using impermeable condition. Material constants for PZT-4 and PZT-5 can be found in Table.1. Fig.8 and Fig.9 give the angular distributions of $D_r\sqrt{r}$ and $D_\theta\sqrt{r}$. Theoretical results of Pak (1992) and Sosa (1992) are also plotted in the figures for comparison. However, the results of Park & Sun (1995) are not shown as their normalizing factors were not specified. All of our data are taken at the element origins closest to $r/a = 3.86\times10^{-3}$. For $r/a = 10^{-4}$ to 10^{-2}, the predicted $D_r\sqrt{r}$ and $D_\theta\sqrt{r}$ remain practically unchanged. In other words, the $1/\sqrt{r}$ -singularities of D_r and D_θ are clearly verified. On the other hand, slight changes in $\sigma_r\sqrt{r}$, $\sigma_\theta\sqrt{r}$ and $\tau_{r\theta}\sqrt{r}$ are observed for $r/a = 10^{-4}$ to 10^{-2}. Nevertheless, the $1/\sqrt{r}$ -singularities of σ_r, σ_θ and $\tau_{r\theta}$ can still be confirmed. It can be seen that the present results are close to the analytical solutions of Pak (1992) and Sosa (1992).

However, the $\sigma_\theta\sqrt{r}$ -distribution is quite different from that presented by Park & Sun (see Fig.3 in Park & Sun, 1995). The latter is similar to the $\sigma_r\sqrt{r}$ -distribution. The invariancy of $D_r\sqrt{r}$, $D_\theta\sqrt{r}$, $\sigma_r\sqrt{r}$, $\sigma_\theta\sqrt{r}$ and $\tau_{r\theta}\sqrt{r}$ within the above range of r is in contrast with the numerical results of Kumar & Singh (1996).

Under the permeable condition, singularities are not noted in D_r and D_θ. The stress predictions are very close to one computed under the impermeable condition. The difference is in the order of 10^{-3} and thus not repeated.

To examine the energy release rate, the following *J*-integral derived by Pak (1990) is computed for the three paths shown in Fig. 4:

$$J = \int_\Gamma (h_e n_x - \sigma_{ij} n_j u_{i,1} + D_i n_i E_1) ds \tag{26}$$

where h_e is the electric enthalpy, (n_x, n_y) constitute the unit outward normal to path Γ, repeated subscripts denote the summation over x and y. For linear material, h_e has the same value as the mechanical enthalpy h_m defined under Eqn.(7). The *J*-integral results are listed in Table 3. It can be noted that both the impermeable and permeable conditions do not affect the path independence of the integral. However, the permeable condition leads to a higher *J*-value. If energy release rate is the governing fracture criterion, the permeable crack is more vulnerable than the impermeable crack under pure mechanical loading.

Table 3. Computed *J*-integrals(in $10^{-11}a$ N/m) for pure mechanical loading(σ_∞=1N/m^2), see Fig.3, 4

crack face idealization	PZT-4			PZT-5		
	path 1	path 2	path 3	path 1	path 2	path 3
impermeable	2.869	2.869	2.871	2.646	2.644	2.655
permeable	3.768	3.758	3.737	3.216	3.209	3.209

<u>*Pure Electric Loading*</u> - In this case, only the far field electric displacement D_∞ is acting. Fig.10 and Fig.11 show the angular distributions of $\sigma_r\sqrt{r}$, $\sigma_\theta\sqrt{r}$ and $\tau_{r\theta}\sqrt{r}$ for PZT-4 and PZT-5 at the crack tip region under the impermeable condition. Fig.12 and Fig.13 give the angular distributions of $D_r\sqrt{r}$ and $D_\theta\sqrt{r}$. Most of the predicted stresses are close to the analytical solutions of Pak (1992) and Sosa (1992) both in distribution and magnitude except that there appear to be magnitude differences in $\sigma_r\sqrt{r}$ for PZT-4 and $\sigma_\theta\sqrt{r}$ for PZT-5. Same as under the pure mechanical loading, the predicted $\sigma_\theta\sqrt{r}$ is quite different from that of Park & Sun (see Fig.3 in Park & Sun, 1995). As

θ increases, Park and Sun's circumferential stress changes from positive to negative but the present one is basically negative for the entire range of θ. Table 4 lists the *J*-integrals which are negative and agree with the results by Pak (1990, 1992) and Park & Sun (1995). In other words, the electric loading always impedes crack propagation if energy release rate is the governing fracture criterion.

Using the permeable condition, the computed electric displacements are uniform over the finite element mesh while the stress is negligible compared to that of the impermeable model (the magnitude ratio ≈ 10^{-9}). Crack tip singularity is not noted and thus the computed *J*-integrals are practically zero. These agree with the conclusions of Dunn (1994) and Sosa & Khutoryansky (1996) in the sense that the electric loading has no effect on crack propagation under the permeable condition regardless whether stress- or energy-based fracture criterion is adopted.

Table 4. Computed *J*-integrals (in $10^{-11}a$ N/m) for pure electric loading(D_∞= 1 μC/m^2), see Fig.3, 4

crack face idealization	PZT-4			PZT-5		
	path 1	path 2	path 3	path 1	path 2	path 3
impermeable	-13.81	-13.77	-13.87	-7.229	-7.208	-7.258
permeable	$\approx 10^{-10}$	$\approx 10^{-10}$	$\approx 10^{-10}$	$\approx 10^{-10}$	$\approx 10^{-10}$	$\approx 10^{-10}$

<u>*Mixed Loading*</u> - In this case, the ratio of the far field electric displacement D_∞ to far field stress σ_∞ is varied. It should be noted that σ_∞ is always kept positive value to avoid crack closure. As noted in the last paragraph, the stress induced by the electric loading is negligible under the permeable condition, only the impermeable condition is considered here. To compare the result with that by Sosa (1992), the following D_∞/σ_∞ 's are considered for PZT-4.

PZT-4: $D_\infty/\sigma_\infty = \pm 10^{-9}, \pm 10^{-8}, \pm 5\times 10^{-8}$

For linear materials, the results for mixed loading can simply be obtained by linear superposition of the predictions obtained from pure mechancial loading and electric loading. As the crack opening or circumferential stress is mostly concerned from the fracture point view, it is plotted for examining whether the crack will deviate from its initial direction. Fig.14 and Fig.15 show the stress in PZT-4 for positive and negative D_∞ 's, respectively. All solutions indicate that the maximum circumference stress will shift away from θ = 0 when a large enough negative D_∞ is applied.

Energy release rate is another concern in fracture mechanics. Pak (1992) and Park & Sun (1995) gave the following formulae for the energy release rates of PZT-5 and PZT-4:

$$G_{PZT-5} = \frac{a}{8}(2.0189 \times 10^{-10}\sigma_\infty^2 + 0.32108 D_\infty \sigma_\infty - 5.7528 \times 10^8 D_\infty^2)\,\text{N/m} \quad \text{by Pak (1992)}$$

$$G_{PZT-4} = \frac{\pi a}{2}(1.48 \times 10^{-11}\sigma_\infty^2 + 0.0534 D_\infty \sigma_\infty - 8.56 \times 10^7 D_\infty^2)\,\text{N/m} \quad \text{by Park \& Sun (1995)}$$

where the half crack length a is in m. The above two relations are plotted in Fig.16 for D_∞/σ_∞ ranging from -10^{-9} to $+10^{-9}$. Within the same range, eleven *J*-integrals are here computed for each material as shown in Fig.16. Based on results, the following energy release rates are obtained by fitting a quadratic curve to our acquired data:

$$G_{PZT-5} = \frac{a}{8}(2.1188 \times 10^{-10}\sigma_\infty^2 + 0.3258 D_\infty \sigma_\infty - 5.7856 \times 10^8 D_\infty^2)\ \text{N/m}$$

$$G_{PZT-4} = \frac{\pi a}{2}(1.8270 \times 10^{-11}\sigma_\infty^2 + 0.04510 D_\infty \sigma_\infty - 8.7949 \times 10^7 D_\infty^2)\ \text{N/m}$$

It can be noted that the two expressions for PZT-5 are very close whilst the ones for PZT-4 are quite different.

4. Conclusions

A piezoelectric hybrid element is formulated for computing the electromechanical coupling problem. In contrast with the conventional displacement-based element, the present hybrid model can efficiently simulate the singularity fields near the crack tip. Since the stress $\boldsymbol{\sigma}$ and the electric displacement **D** are taken as independent variables in the element formulation.

Under the impermeable crack condition, the present finite element solutions reproduce the $1/\sqrt{r}$ -singularity of the angular distributions for $\boldsymbol{\sigma}$ and **D** at the crack tip zone, and no matter which kind of loading (mechanical, electrical or mixed one) is considered, such that some theoretical solutions of concern are verified numerically.

The computed results indicate that under the impermeable condition, the mechanical loading (σ_∞) will induce crack propagation in its initial direction. On the contrary, the negative electric loading ($-D_\infty$) may induce the crack deviates from its initial direction when the electric displacement becomes a governing loading.

The numerical solutions under the permeable condition show that in the case of pure mechanical loading, the stresses $\boldsymbol{\sigma}$ still hold the $1/\sqrt{r}$ -singularity at the crack tip zone, but the singularity of the electric displacements **D** will disappear. On the other hand, in the case of pure electric loading,

the computed **D** take a uniform distribution, while σ and the J-integral /the energy release rate are practically zero.

Pak et al's energy release rate formulas are well examined by means of the calculations of J integral in the paper. The suggested numerical fitting approach can also be developed to seek some approximate energy formulas for various piezoelectric crack problems with the typical $\boldsymbol{\sigma}_\infty \sim \mathbf{D}_\infty$ coupling solutions.

Acknowledgments

The financial support of *the University of Hong Kong* in form of a CRCG grant and the assistance from the *National Natural Science Foundation of China* through project No. 19772051 are gratefully acknowledged.

References

Dunn, M. L. (1994) The effects of crack face boundary conditions on the fracture mechanics of piezoelectric solids. *Eng.Frac.Mech.* **48**, 25-39.

EerNisse, E. P. (1983) Variational method for electroelastic vibration analysis. *IEEE Trans. - J. Sonics & Ultrasonics* **14**, 59-67.

Jackson, J. D. (1976) *Classical Electrodynamics*. John Wiley, New York.

Kumar, S. and Singh, R. N. (1996) Crack propagation in piezoelectric materials under combined mechanical and electrical loadings. *Acta Mater.* **44**, 173-200.

Kumar, S. and Singh, R. N. (1997) Energy release rate and crack propagation in piezoelectric materials. Part I: mechanical/electrical load, Part II: combined mechanical and electrical loads. *Acta Mater.*, **45**, 849-868.

Liu, M. (1998) *Finite Element Analysis for Cracked Piezoelectric Medium*. M. Sc. Thesis, Dept. of Modern Mechanics, Univ. of Sci. & Tech. of China, Hefei.

Pak, Y. E. (1990) Crack extension force in a piezoelectric material. *J.Appl.Mech.* **57**, 647-653.

Pak, Y. E. (1992) Linear electro-elastic fracture mechanics of piezoelectric materials. *Int.J.Frac.* **54**, 79-100.

Park, S. B. and Sun, C. T. (1995) Effect of electric field on fracture of piezoelectric ceramics. *Int.J.Frac.* **70**, 203-216.

Parton, V. Z. (1976) Fracture mechanics of piezoelectric materials. *Acta Astronaut.* **3**, 671-683. Deeg, W. F. (1980) *The analysis of dislocation, crack and inclusion problems in piezoelectric solids*. Ph.D. dissertation, Stanford University, CA.

Pian, T. H. H. and Sumihara, K. (1984) Rational approach for assumed stress finite elements. *Inter.J.Numer.Methods Engrg.* **20**, 1685-1695.

Pian, T. H. H. and Wu, C. C. (1988) A rational approach for choosing stress term for hybrid finite element formulations. *Inter.J.Numer.Methods Engrg.* **26**, 2331-2343.

Sosa, H. (1992) On the fracture mechanics of piezoelectric solids. *Int.J.Solids Struct.* **29**, 2613-2622.

Sosa, H. and Khutoryansky, N. (1996) New developments concerning piezoelectric materials with defects. *Int.J.Solids Struct.* **33**, 3399-3414.

Sze, K. Y. (1992) Efficient formulation of robust hybrid elements using orthogonal stress/strain interpolants and admissible matrix formulation. *Inter.J.Numerical Methods Engrg.* **35**, 1-20.

Wu, C. C. and Cheung, Y. K. (1995) On optimization approach of hybrid stress elements, *Finite Elements in Analysis & Design* **21**, 111-128.

List of Figures

Fig.1. Description of the four-node piezoelectric plane element

Fig.2. A unit thickness PZT-4 plane strain cantilever beam under pure bending

Fig.3. A centrally cracked piezoelectric tensile plane strain panel of dimension $w \times w$, half crack length a and $w/a = 8$

Fig.4. Finite element mesh for the upper right hand quarter of the panel shown in Fig.2, J-integrals are computed along the three highlighted paths

Fig.5. Enlarged view of the finite element mesh at the crack tip

Fig.6. Angular distributions of stresses for PZT-4 under mechanical loading and impermeable condition

Fig.7. Angular distributions of stresses for PZT-5 under pure mechanical loading and impermeable condition

Fig.8. Angular distribution of electric displacements for PZT-4 under pure mechanical loading and impermeable condition

Fig.9. Angular distribution of electric displacements for PZT-5 under pure mechanical loading and impermeable condition

Fig.10. Angular distribution of stresses for PZT-4 under pure electric loading and impermeable condition

Fig.11. Angular distribution of stresses for PZT-5 under pure electric loading and impermeable condition

Fig.12. Angular distribution of electric displacements for PZT-4 under pure electric loading and impermeable condition

Fig.13. Angular distribution of electric displacements for PZT-5 under pure electric loading and impermeable condition

Fig.14. Effect of positive D_∞'s on the angular distribution of circumferential stress in PZT-4 under mixed loading and impermeable condition

Fig.15. Effect of negative D_∞'s on the angular distribution of circumferential stress in PZT-4 under mixed loading and impermeable condition

Fig.16. J-integrals verus D_∞ / σ_∞

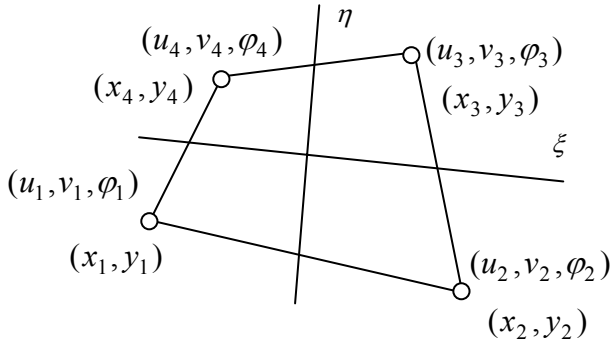

Fig.1. Description of the four-node piezoelectric plane element.

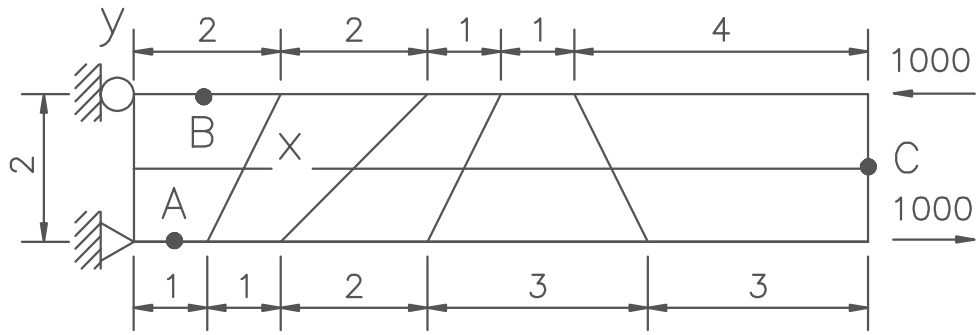

Fig.2. A unit thickness PZT-4 plane strain cantilever beam under pure bending.

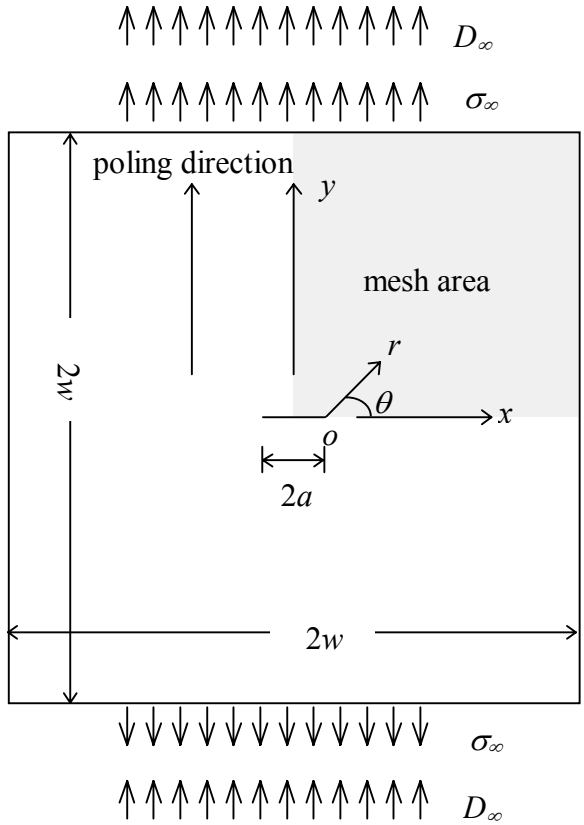

Fig.3. A centrally cracked piezoelectric tensile plane strain panel of dimension $w \times w$, half crack length a and $w/a = 8$.

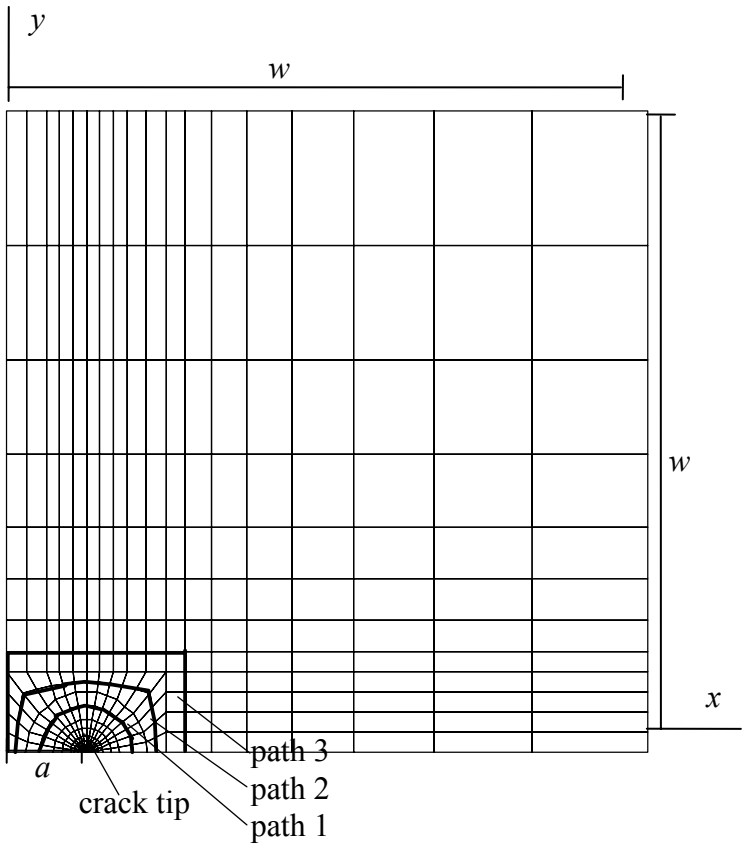

Fig.4. Finite element mesh for the upper right hand quarter of the panel shown in Fig.2, J-integrals are computed along the three highlighted paths

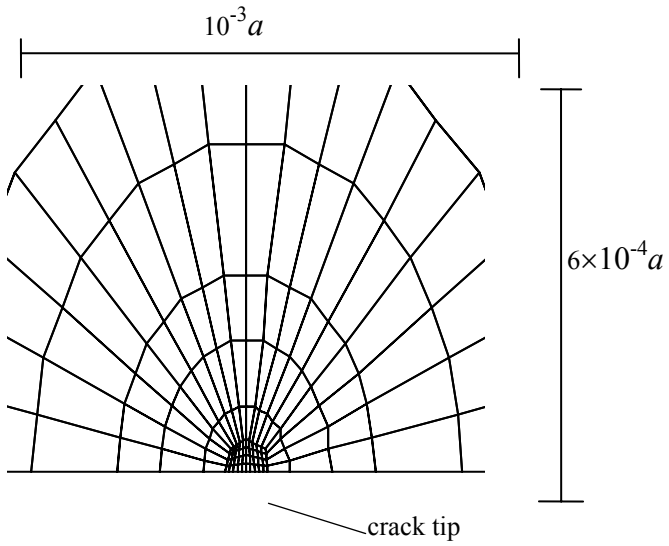

Fig.5. Enlarged view of the finite element mesh at the crack tip

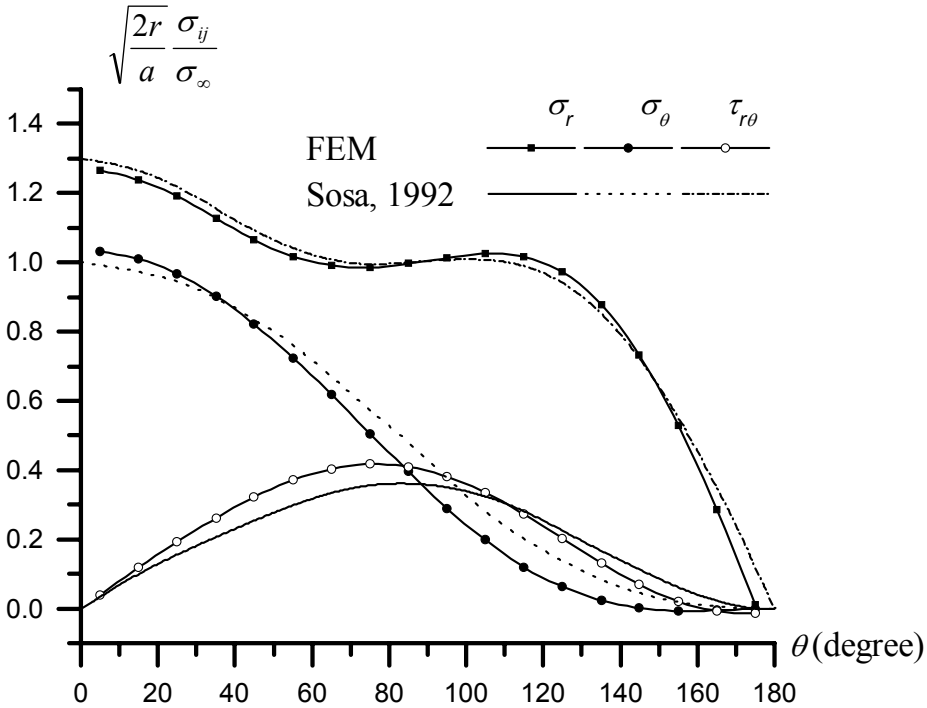

Fig.6. Angular distributions of stresses for PZT-4 under mechanical loading and impermeable condition

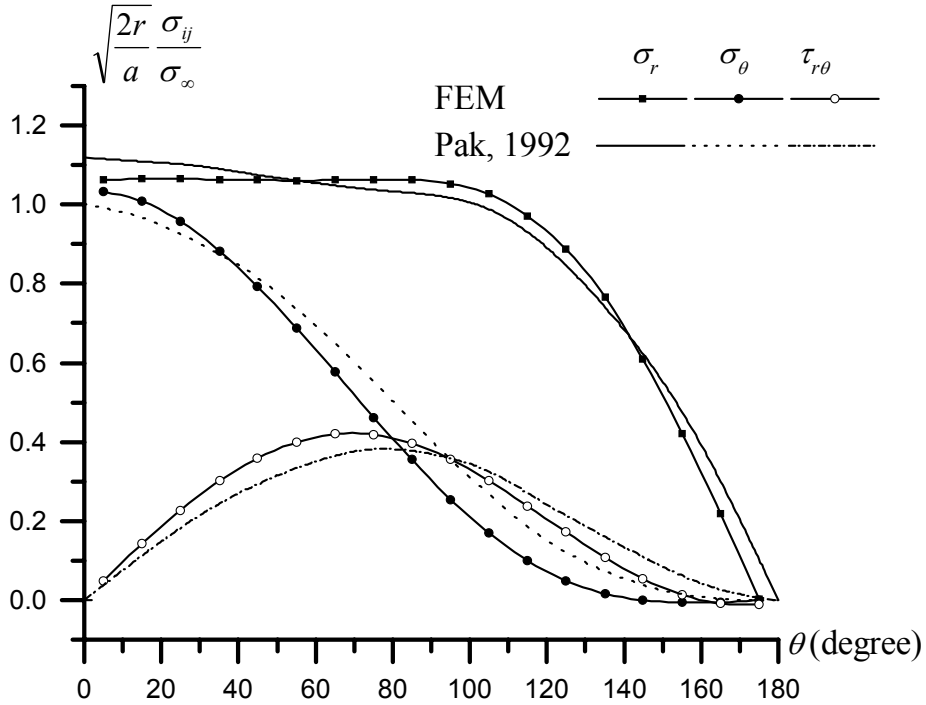

Fig.7. Angular distributions of stresses for PZT-5 under pure mechanical loading and impermeable condition

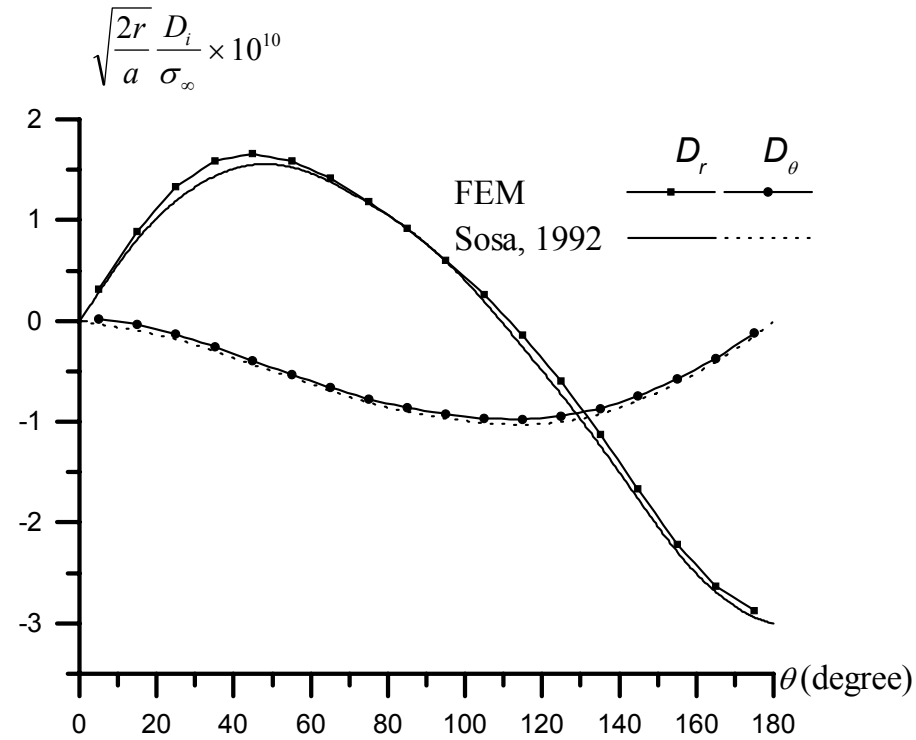

Fig.8. Angular distribution of electric displacements for PZT-4 under pure mechanical loading and impermeable condition

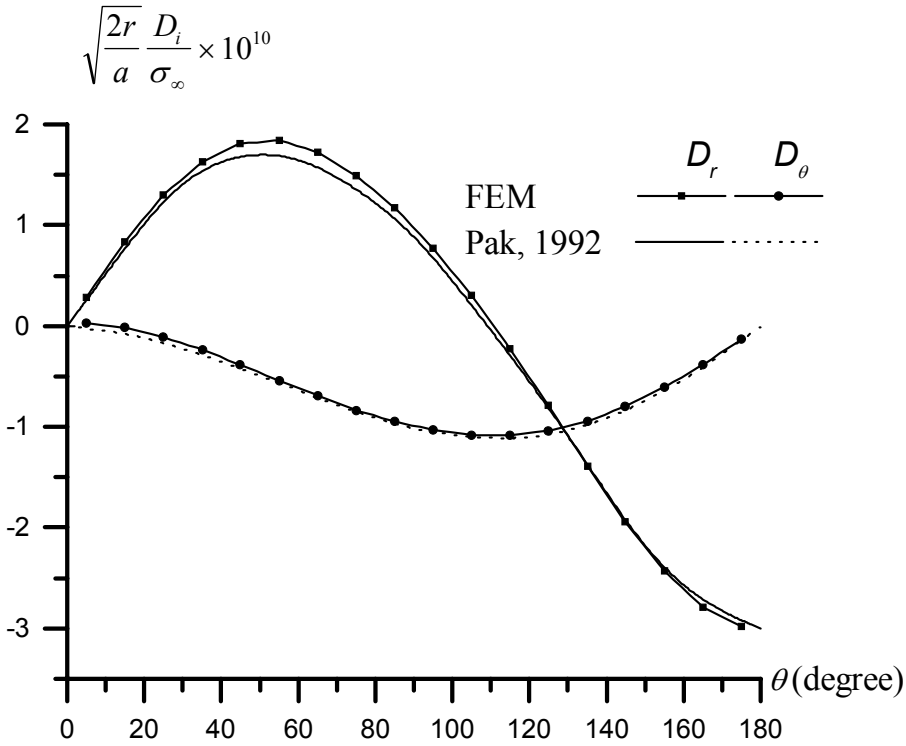

Fig.9. Angular distribution of electric displacements for PZT-5 under pure mechanical loading and impermeable condition

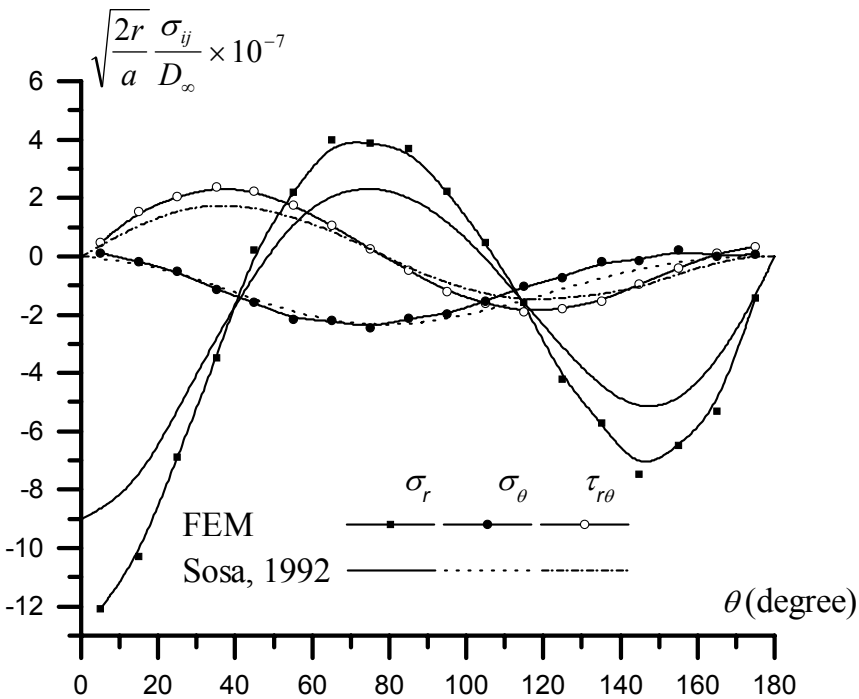

Fig.10. Angular distribution of stresses for PZT-4 under pure electric loading and impermeable condition

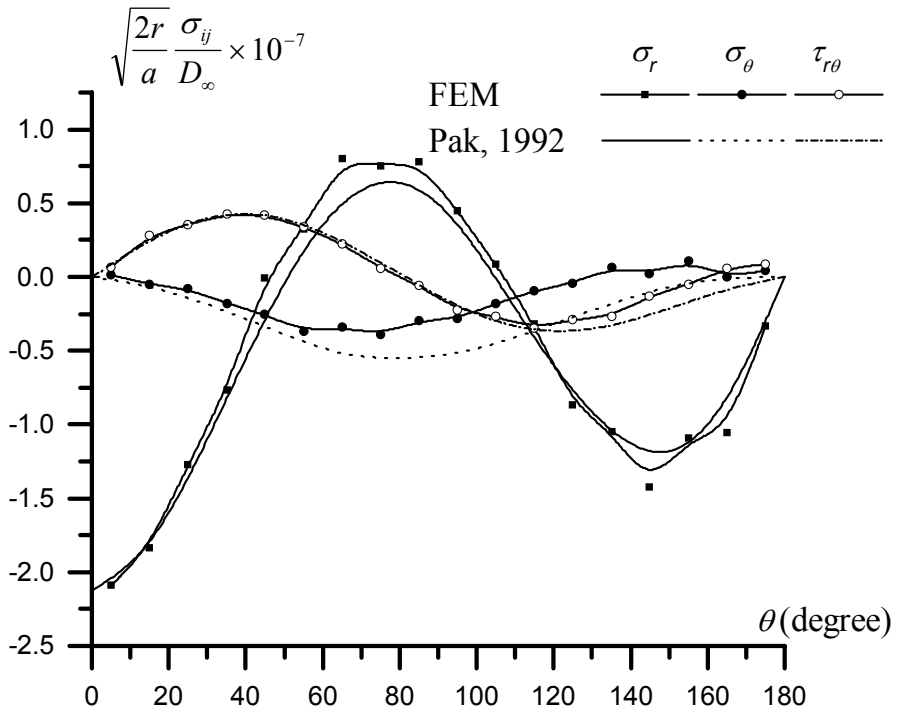

Fig.11. Angular distribution of stresses for PZT-5 under pure electric loading and impermeable condition

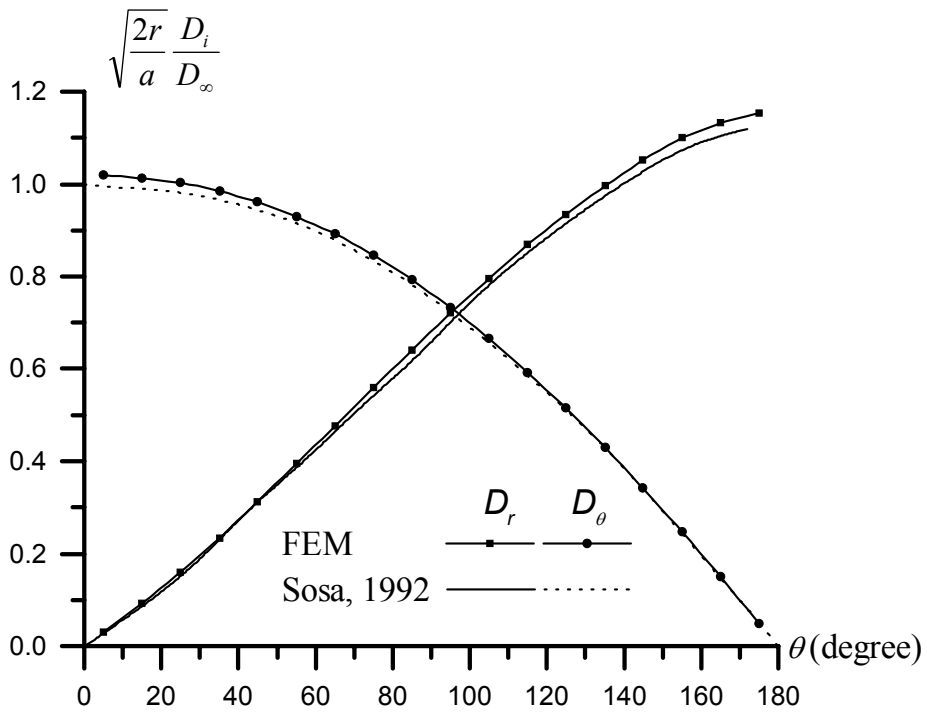

Fig.12. Angular distribution of electric displacements for PZT-4 under pure electric loading and impermeable condition

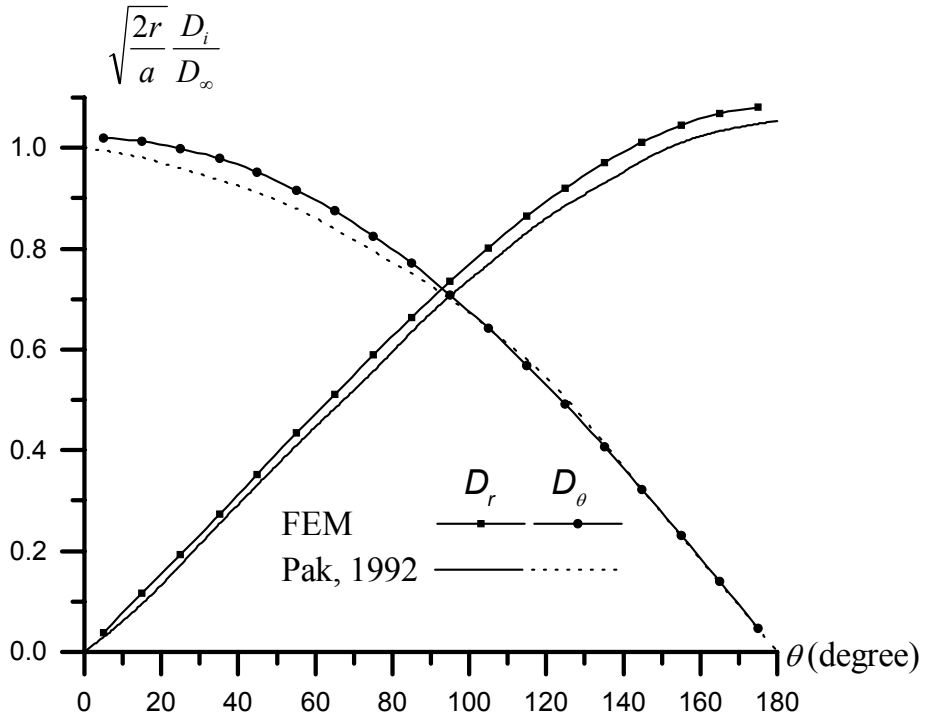

Fig.13. Angular distribution of electric displacements for PZT-5 under pure electric loading and impermeable condition

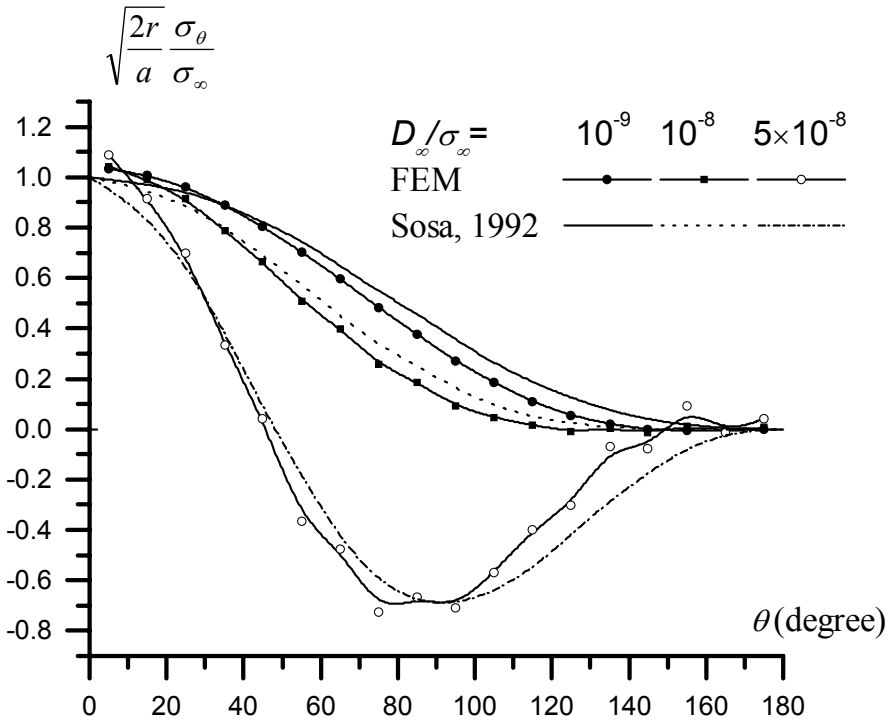

Fig.14. Effect of positive D_∞ 's on the angular distribution of circumferential stress in PZT-4 under mixed loading and impermeable condition

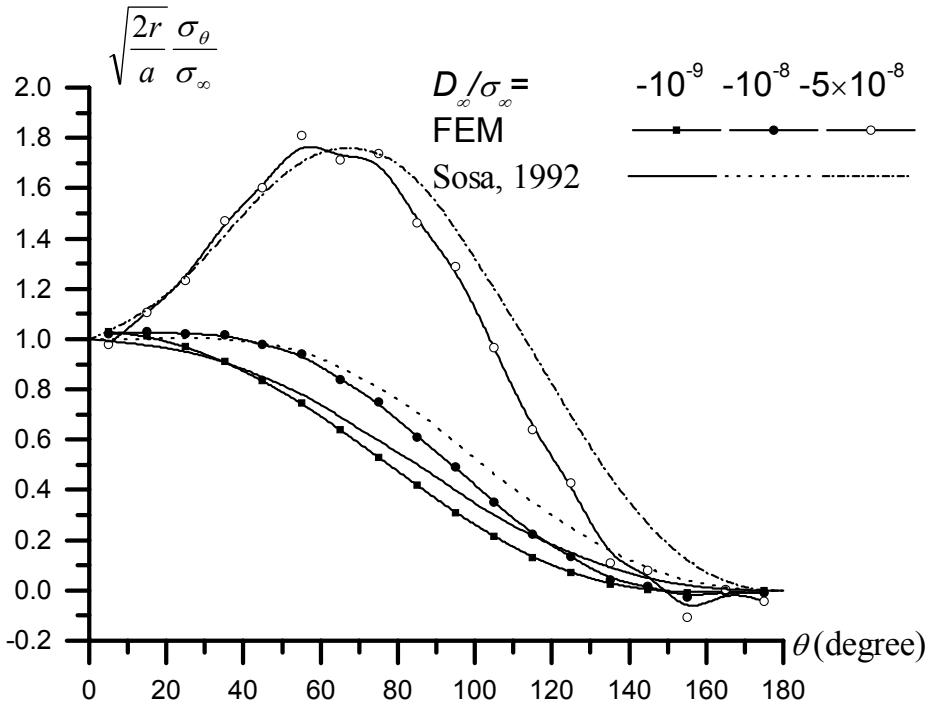

Fig.15. Effect of negative D_∞'s on the angular distribution of circumferential stress in PZT-4 under mixed loading and impermeable condition

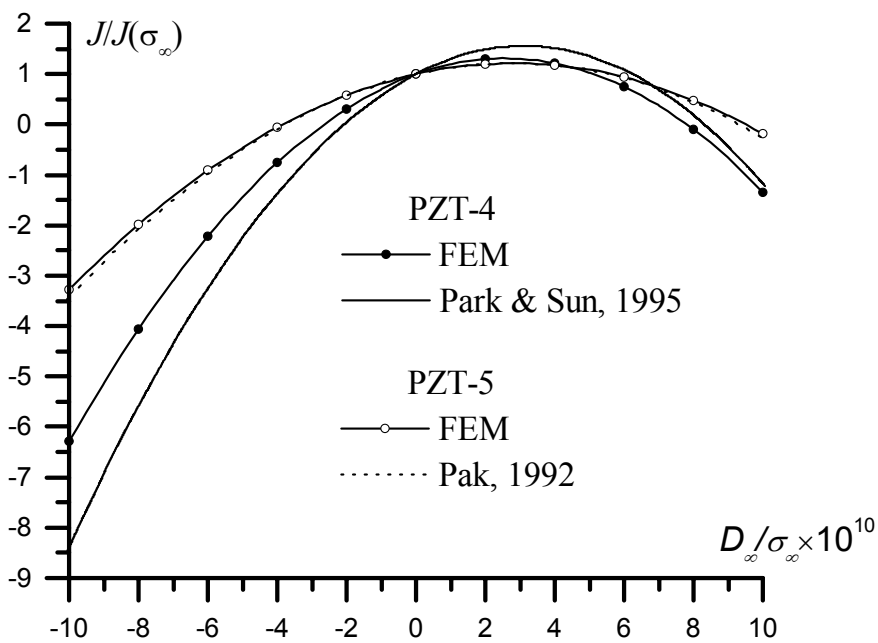

Fig.16. J-integrals verus D_∞/σ_∞